Image-based Inverse Characterization of In-situ Microscopic Composite Properties

Zimu Su[1], Nelson Carvalho[2], Michael W. Czabaj[3], Caglar Oskay[1*]

[1*]Department of Civil and Environmental Engineering, Vanderbilt University, VU Station B#351831, 2301 Vanderbilt Place, Nashville, 37235, TN, US.
[2]Langley Research Center, NASA, 1 NASA Dr, Hampton, 23681, VA, US.
[3]Department of Mechanical Engineering, University of Utah, 1495 East 100 South 1550 MEK, Salt Lake City, 84112, Utah, US.

*Corresponding author(s). E-mail(s): caglar.oskay@vanderbilt.edu;
Contributing authors: zimu.su@hotmail.com; nelson.carvalho@nasa.gov; m.czabaj@utah.edu;

Abstract

An inverse characterization approach to identify the in-situ elastic properties of composite constituent materials is developed. The approach relies on displacement measurements available from image-based measurement techniques such as digital image correlation and template matching. An optimization problem is formulated, where the parameters of an assumed functional form describing spatially variable material properties are obtained by minimizing the discrepancies between noisy displacement measurements and the corresponding simulated values. The proposed formulation is analyzed from a statistical inference theory standpoint. It is shown that the approach exhibits estimation consistency, i.e. given noisy input data the identified material properties converge to the true material properties as the number of available measurements increases. The performance of the proposed approach is evaluated by a series of virtual characterizations that mimic physical characterization tests in which fiber centroid displacements are obtained through fiber template matching. The virtual characterizations demonstrate that the effect of measurement noise in identifying the in-situ constituent properties can be mitigated by selecting a sufficiently large measurement dataset. The numerical studies also show that, given a rich measurement dataset, the proposed approach is able to describe increasingly complex spatial variation of properties.

Keywords: Inverse characterization, In-situ property, Composite, Spatial variability, Noise effect, Statistical consistency, Template matching.

1 Introduction

Micromechanical analysis and multiscale modeling of composite materials have received substantial attention because of their potential to describe the fundamental mechanisms of mechanical and failure response [41, 44, 46], including the effect of material variability and associated uncertainty across length scales [5, 6, 38], and inform models that aim to predict response and failure of composite structures [32, 40]. The combined fundamental mechanistic understanding and predictive modeling capability have the potential to help improve composite materials and designs. Microstructural analysis and multiscale modeling techniques for composites rely on the availability of (a) morphological information on material microstructure; and (b) properties of the constituent materials as they pertain to the mechanical regime of interest (i.e., elastic moduli, thermal conductivity, strength, toughness, etc.). The effect of microstructural morphology on the mechanical behavior of composites has been subject to previous studies (e.g. [37]). In these studies, the effect of the microstructural morphology is typically investigated using digital numerical models constructed based directly on micrographs of the material (digital twins) or indirectly based on a statistical description of the microstructure. Careful characterization of the properties of the constituents and their spatial variation across the composite volume at the microscale, on the other hand, has received relatively less attention. The spatial variability of the constituent properties can be due to chemical interactions between bonding agents and composite constituents [19, 25]; non-uniform cross-linking that results from variations in curing temperature and polymerization [1, 34], and others.

The properties of the constituents used in micromechanical or multiscale analysis are typically identified by a combination of (1) inverse calibration informed by experiments at a larger scale [3, 4, 12, 13, 30, 31]; and (2) ex-situ experiments that isolate a specific property (e.g., fiber pullout for shear dominated interface failure [53] and fiber tensile testing [43]). In certain cases, molecular dynamics have also been employed to estimate constituent properties of some materials [18, 41]. A number of complicating factors hinder the characterization of the properties of the constituents. The composite constituents can exhibit significant differences in their in-situ and ex-situ properties [19, 21, 33], therefore relying purely on ex-situ experimentation to characterize all properties may lead to inaccurate predictions. The measured in-situ modulus of a composite resin has been shown to differ by as much as 30% when compared to the ex-situ (neat polymer) determined value [19]. Such a difference would result in a proportional difference in stress and hence damage onset prediction. Besides, inverse calibration with experiments at larger scale often results in non-unique material properties, contributing to prediction uncertainty. Furthermore, all experiments exhibit a certain amount of measurement noise that could lead to erroneous properties, the magnitude of which is seldom quantified.

Characterization of the properties of the constituents based on in-situ experiments at the microscale offers an alternative approach. Nanoidentation testing probes the substrate of individual constituents within a small localized region and has been employed to investigate the in-situ properties of composite materials including the Young's modulus [19, 21], plasticity parameters [35], and viscoplasticity parameters [33]. The spatial variation of resin Young's modulus has also been observed at fiber-resin interphase regions (e.g. [24, 25] in polymer matrix composite). Hardiman et al [21] observed that the variation in Young's modulus is related to the size of resin pockets in a carbon fiber reinforced polymer (CFRP). Measuring resin properties using nanoindentation requires a strategy to account for the effect of fiber constraints [21, 22]. The presence of fibers and their possible contact with the indenter tip can lead common indentation calibration methods (e.g. continuous stiffness measurement technique) to overestimate the resin properties [20].

Image-based measurement techniques, such as digital image correlation (DIC) [9, 10, 28, 42], digital volume correlation (DVC, i.e., 3D extension of DIC) [29], and fiber template matching (FTM) [11] have been applied to measure deformations and strains complementing and/or replacing more traditional methods such as strain gauges. Combining high-magnification microscopy and high-resolution digital imaging, microscale image-based methods have been used to measure displacements and strain fields at the microscale in composite materials with or without the presence of failure [9, 10, 28, 42]. In [19, 21], significant discrepancies were found when correlating displacements measured at the microscale to simulations performed using ex-situ properties of the bulk material. This result aligns with the findings from the nanoindentation studies discussed previously, and with the notion that in-situ properties may differ from their ex-situ counterparts.

The key novelty of this study is the proposal and study of a statistically consistent framework to obtain in-situ, spatially variable, elastic properties of composite materials using noisy image-based displacement measurements obtained at the microscale. While inverse estimation approaches have been previously explored and investigated to characterize the in-situ material properties for the applications, such as structural health monitoring (e.g. [47, 49]) and soft tissue elastography(e.g. [16, 51]), this study focuses on the inverse characterization of in-situ elastic properties of composite constituent materials based on microscopic displacement measurements. The characterization follows an optimization procedure, in which the discrepancy between observed and simulated microscale displacements are minimized to arrive at the properties of the constituents. As evidenced by nano-indentation tests, the resin properties can exhibit spatial variability that may be described by functional forms [21]. In the present work, the parameters of these functional forms are cast as the parameters to be identified through the optimization procedure.

A central aspect of this study is assessing the accuracy of the approach when using noisy input data, which can corrupt the parameter identification process [47]. Bayesian inference has been used in the literature to manage the effect of measurement noise on the parameter identification by quantifying uncertainty in the identified parameters. Uncertainty in the parameter identification process can be quantified by obtaining a stable posterior distribution of the model prediction through a Markov sampling approach. Instead of Bayesian approach, as a first step and in order to avoid the computational cost of Monte Carlo-based sampling methods, the present study uses statistical inference theory [2, 23] to study and quantify the effect of measurement noise. Using statistical inference arguments [2, 23], the approach is shown to exhibit estimation consistency. Estimation consistency is defined as the convergence of the parameters identified by the approach to the true parameters with an increase in the number of measurements used. The effectiveness of the proposed characterization method is evaluated by a series of virtual characterizations of the properties of the constituents of a microscopic continuous fiber-reinforced composite specimen. The input displacement measurements used in the virtual characterizations, referred to as synthetic experimental data, are extracted from the fiber centroids of numerical simulations, performed with assumed constituent properties. These synthetic input datasets aim to mimic the datasets obtained using FTM. The effect of noise is studied by adding different levels of random noise to the noise free synthetic experimental data and comparing the identified properties to the properties assumed in the numerical simulations. The virtual characterizations demonstrate the effect of measurement noise on the fidelity of identified properties. Conditions that reduce the effect of noise on the accuracy of the identified properties are studied.

The remainder of this manuscript is organized as follows: in Section 2, the problem statement and the elements of the inverse identification approach are presented followed by a discussion of the conditions required for the estimation consistency of the approach. In Section 3, the results of several virtual characterizations are reported, documenting the accuracy of the proposed method and assessing the effects of measurement noise level and dataset size. A summary of the work performed and key conclusions are provided in Section 4. Appendix A discusses the conditions of objective function minimization with noise. Appendix B demonstrates the strict convexity of the forward problem as a requisite of statistical consistency. Appendix C provides an analysis of a one-dimensional composite specimen, which is used to discuss the identifiability parameters based on a set of discrete displacement measurements.

2 Inverse characterization methodology

2.1 Problem statement

Consider a long fiber-reinforced composite specimen at the mesoscale with the domain, Ω, parameterized by the position coordinate vector, $\mathbf{y}$. The specimen is subjected to loading, $F(\mathbf{y})$, applied in the transverse plane (i.e. y_1 - y_2 plane shown in Fig. 1). The domain includes n_{f} randomly positioned fibers. The elastic properties of the fibers have been typically assumed to be unaffected by curing in polymer matrix composites (PMCs), e.g. [17]. Therefore, in the present study, the elastic properties of each fiber are taken to be spatially constant, and fiber-to-fiber property variability is assumed to be negligible. This study focuses on the characterization of the resin, since its properties are known to vary spatially in-situ [11] and are a function of the curing conditions [17]. The elastic properties of the resin are taken to exhibit deterministic spatial variability dictated by the manufacturing processes. Potential stochastic variability in the material properties is considered to be small relative to deterministic variability. Under the action of mechanical loading, the composite specimen deforms elastically. A discrete set of displacement measurements are collected on the specimen surface, Γ, which is parallel to the transverse plane: $\mathbf{u}^{\text{mes}} = \{\mathbf{u}_i^{\text{mes}}\}$, with $i = 1, 2 \ldots n$, where n denotes the total number of available displacement observations. Each displacement measurement, $\mathbf{u}_i^{\text{mes}}$, could be the displacement vector (i.e., $\mathbf{u}_i^{\text{mes}} = \{u_{y_1 i}^{\text{mes}}, u_{y_2 i}^{\text{mes}}\}^T$) at a discrete spatial position in the specimen or a generalized displacement (e.g., $\mathbf{u}_i^{\text{mes}} = \int_\Gamma \nu_i(\mathbf{y})\mathbf{U}_i^{\text{mes}}(\mathbf{y})\mathrm{d}\Gamma$, where ν_i is a weight function). Each measurement data point is considered to be noisy due to inaccuracies in the measurement system. We can further generalize experimental data to be a set of observations from n_{exp} experiments. All n_{exp} experiments could be performed on the same specimen (e.g., load-unload-reload cycles with each load-up resulting in a different dataset due to a different load amplitude applied in each cycle or to measurement noise, see Section 2.2); each experiment performed on a different specimen; or a combination thereof. Based on the aforementioned problem description, we seek to estimate the spatially variable elastic properties of the material constituents based on the displacement information.

Figure 1 schematically depicts the estimation approach, where material property estimation is posed as an optimization problem. In order to operate in a finite dimensional setting, the spatially varying elastic properties are expressed using a function $\mathbf{g}(\mathbf{y}; \boldsymbol{\theta})$, $\mathbf{y} \in \Omega$, where $\boldsymbol{\theta} \in \boldsymbol{\Theta}$ is a vector of parameters. The "true" set of material properties that we seek to identify is denoted as $\hat{\boldsymbol{\theta}} \in \boldsymbol{\Theta}$. The displacement measurements, $\mathbf{u}^{\text{mes}}$, are the input to the optimization procedure. Numerical simulation of the mechanical response of the specimen constitutes the "forward problem". The optimization procedure iteratively adjusts the constitutive parameter vector, $\boldsymbol{\theta}$, until the discrepancy between the computationally obtained displacement measures, $\mathbf{u}^{\text{sim}} = \{\mathbf{u}_i^{\text{sim}}\}$ with $i = 1, 2 \ldots n$, and the experimental observations is minimized. The prediction error, $\mathscr{L}_n$ (also referred to as the objective function, cost or risk function), adopts the form of normalized mean square error (NMSE):

$$\mathscr{L}_n(\boldsymbol{\theta}) = \frac{\sum_{i=1}^n \|\mathbf{u}_i^{\text{mes}} - \mathbf{u}_i^{\text{sim}}(\boldsymbol{\theta})\|^2}{\sum_{i=1}^n \|\mathbf{u}_i^{\text{mes}}\|^2} \tag{1}$$

where $\|\cdot\|$ stands for the l^2-norm and $\mathbf{u}_i^{\text{sim}}$ is obtained from the forward problem, which minimizes the potential energy Π_p with model parameters, $\boldsymbol{\theta}$, and load, $\mathbf{F}$, as the inputs:

$$\mathbf{U}^{\text{sim}} = \arg\min_{\hat{\mathbf{U}}^{\text{sim}}} \Pi_p\left(\hat{\mathbf{U}}^{\text{sim}}; \boldsymbol{\theta}, \mathbf{F}\right) \tag{2}$$

where $\hat{\mathbf{U}}^{\text{sim}}$ represents any kinematically admissible displacement field. The simulated displacement field, $\mathbf{U}^{\text{sim}}$, is then sampled to obtain $\mathbf{u}^{\text{sim}}$ for discrete values that correspond to measured data. The model estimate, $\hat{\boldsymbol{\theta}}_n$, is obtained from Eq. 1 as:

$$\hat{\boldsymbol{\theta}}_n = \arg\min_{\boldsymbol{\theta}} \mathscr{L}_n(\boldsymbol{\theta}) \tag{3}$$

In Section 2.2, the conditions in which one can guarantee that there is a unique model estimate that satisfies Eq. 3 and converges to the true model parameters are discussed. Particular attention is given to the effect of measurement noise.

2.2 Optimization with noisy data

The accuracy of the solution to the optimization problem (Eq. 3) depends on the following factors: (1) the measurement noise level, indicated by the standard deviation; (2) the amount of experimental observations, n; and (3) the inference of the material model, such as assumption of the functional form describing the spatial variability of the properties, $\mathbf{g}(\mathbf{y}; \boldsymbol{\theta})$. In what follows, we focus on the effect of measurement noise and assume that the model error is insignificant compared with the measurement noise. In the statistical inference theory [23], the proposed objective function leads to estimates of unknown parameters, $\hat{\boldsymbol{\theta}}_n$, that asymptotically converge to the true values, $\hat{\boldsymbol{\theta}}$, with an increasing amount of measurement data. Following the nomenclature proposed in [2], the

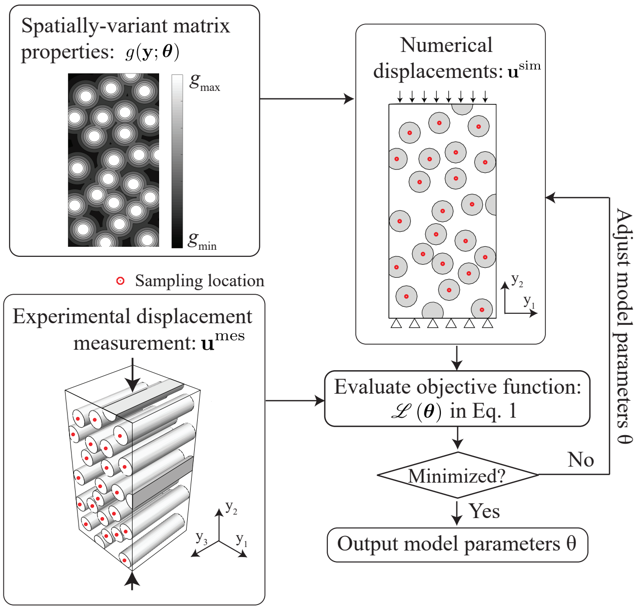

Fig. 1: Schematic illustration of characterization for in-situ microscopic epoxy resin properties using optimization approach.

risk consistency of the model estimate is defined as the convergence of objective function with $\hat{\boldsymbol{\theta}}_n$ to the minimum value in probability:

$$\mathscr{L}(\hat{\boldsymbol{\theta}}_n) \xrightarrow{p} \min\left\{\mathscr{L}(\boldsymbol{\theta}) | \boldsymbol{\theta} \in \boldsymbol{\Theta}\right\} \tag{4}$$

with $\mathscr{L}$ indicating the objective function described by the expectation, $\mathbb{E}$, of the continuous displacement field:

$$\mathscr{L}(\boldsymbol{\theta}) = \frac{\mathbb{E}\left[\|\mathbf{U}(\mathbf{y}) + \zeta(\mathbf{y}) - \mathbf{U}^{\mathrm{sim}}(\mathbf{y}; \hat{\boldsymbol{\theta}})\|^2\right]}{\mathbb{E}\left[\|\mathbf{U}(\mathbf{y}) + \zeta(\mathbf{y})\|^2\right]} \tag{5}$$

where $\mathbf{U}(\mathbf{y})$ denotes the true displacement field and ζ is a Gaussian random field associated with the measurement noise. $\mathbf{U}(\mathbf{y})$ is not directly accessible since any attempt of measurement will include a measure of noise captured by ζ. Since the model error is assumed to be negligible, the simulation predicts the true displacement field when the true set of parameter values are used: $\mathbf{U}^{\mathrm{sim}}(\mathbf{y}; \hat{\boldsymbol{\theta}}) = \mathbf{U}(\mathbf{y})$. Risk consistency indicates that the prediction error made based on the discrete displacement measurements leads asymptotically (i.e., $n \to \infty$) to the smallest prediction error in the continuum sense, since $\mathscr{L}$ is the risk function associated with the continuous displacement fields.

In discrete form, the set of displacement measurements $\mathbf{u}^{\mathrm{mes}}$ consists of the true displacement values, $\mathbf{u}$, sampled from $\mathbf{U}$, and the measurement noise term, $\boldsymbol{\epsilon}$, that are realizations of ζ taken at the measurement points:

$$\mathbf{u}^{\mathrm{mes}} = \mathbf{u} + \boldsymbol{\epsilon} \tag{6}$$

where $\boldsymbol{\epsilon}$ is the vector of independent and identically distributed random variables associated with each displacement measurement (i.e., the measurement noise is taken to be spatially uncorrelated). Each error component is assumed to follow a certain probability distribution with zero mean ($\mathbb{E}(\epsilon_{y_1}) = \mathbb{E}(\epsilon_{y_2}) = 0$) and the variance of $\mathbb{E}(\epsilon_{y_1}) = \mathbb{E}(\epsilon_{y_2}) = \sigma_\epsilon^2$. We note that no spatial correlation and zero-mean (i.e., lack of bias) assumptions may not necessarily hold for all measurement types, and are used in the exemplar cases discussed in this manuscript. Some prior studies considered no spatial correlation when the imaging system gains the RAW data without any preprocessing [50, 52]. Furthermore, characterization of the true distribution of noise could be difficult to determine and likely dependent on the material imaged and the type of the imaging system used.

In the objective function formulation (Eq. 1), the random noise term can be condensed out by substituting Eq. 6:

$$\mathscr{L}_n(\boldsymbol{\theta}) = \frac{\frac{1}{n}\left[\sum_{i=1}^{n} \|\boldsymbol{\eta}_i(\boldsymbol{\theta})\|^2 + 2\boldsymbol{\epsilon}_i \cdot \boldsymbol{\eta}_i(\boldsymbol{\theta}) + \|\boldsymbol{\epsilon}_i\|^2\right]}{\frac{1}{n}\left[\sum_{i=1}^{n} \|\mathbf{u}_i\|^2 + 2\boldsymbol{\epsilon}_i \cdot \mathbf{u}_i + \|\boldsymbol{\epsilon}_i\|^2\right]} = \frac{\overline{\|\boldsymbol{\eta}_n(\boldsymbol{\theta})\|^2} + 2\overline{\boldsymbol{\epsilon}_n \cdot \boldsymbol{\eta}_n(\boldsymbol{\theta})} + \overline{\|\boldsymbol{\epsilon}_n\|^2}}{\overline{\|\mathbf{u}_n\|^2} + 2\overline{\boldsymbol{\epsilon}_n \cdot \mathbf{u}_n} + \overline{\|\boldsymbol{\epsilon}_n\|^2}} \tag{7}$$

where the numerator and denominator were multiplied by $1/n$, the overbar notation indicates sample averaging, and $\boldsymbol{\eta}_i(\boldsymbol{\theta}) = \mathbf{u}_i - \mathbf{u}_i^{\text{sim}}(\boldsymbol{\theta})$. $\overline{\|\boldsymbol{\eta}_n(\boldsymbol{\theta})\|^2}$ is the deterministic prediction error between the true and simulated displacement values. In Appendix A, it is shown that minimizing $\mathscr{L}_n$ does not necessarily minimize the deterministic prediction error due to the effect of measurement noise except at the asymptotic limit.

Leveraging the law of large numbers ($n \to \infty$) enables the summation of the noise terms $\boldsymbol{\epsilon}_i$ in Eq. 7 to approach their expectation and the square of them to their variance:

$$\frac{1}{n}\sum_{i=1}^{n} \boldsymbol{\epsilon}_i \cdot \boldsymbol{\eta}_i(\boldsymbol{\theta}) \to \mathbb{E}(\boldsymbol{\epsilon}_i) \cdot \overline{\boldsymbol{\eta}_n(\boldsymbol{\theta})} = 0 \tag{8}$$

$$\frac{1}{n}\sum_{i=1}^{n} \|\boldsymbol{\epsilon}_i\|^2 \to \mathbb{E}\left(\|\boldsymbol{\epsilon}_i\|^2\right) = \mathbb{E}(\epsilon_{y_1}^2) + \mathbb{E}(\epsilon_{y_2}^2) = 2\sigma_\epsilon^2 \tag{9}$$

$$\frac{1}{n}\sum_{i=1}^{n} \boldsymbol{\epsilon}_i \cdot \mathbf{u}_i \to \mathbb{E}(\boldsymbol{\epsilon}_i) \cdot \overline{\mathbf{u}_n} = 0 \tag{10}$$

noting that the noise term is independent of the true displacements $\mathbf{u}_i$ and the prediction error $\boldsymbol{\eta}_i$.

Substituting Eqs. 8-10 into Eq. 7 and letting $n \to \infty$, the objective function asymptotically converges to:

$$\mathscr{L}_n \to \mathscr{L}_\infty := \frac{\overline{\|\boldsymbol{\eta}_n(\boldsymbol{\theta})\|^2} + 2\sigma_\epsilon^2}{\overline{\|\mathbf{u}_n\|^2} + 2\sigma_\epsilon^2} \tag{11}$$

The value of $\mathscr{L}_\infty$ when evaluated with the true parameter set is:

$$\mathscr{L}_\infty(\boldsymbol{\theta} = \hat{\boldsymbol{\theta}}) = \frac{2\sigma_\epsilon^2}{\mathbb{E}\left(\|\mathbf{u}_i\|^2\right) + 2\sigma_\epsilon^2} \tag{12}$$

since $\mathbf{u}^{\text{sim}}(\hat{\boldsymbol{\theta}}) = \mathbf{u}$, which is the global minimum ($\overline{\|\boldsymbol{\eta}_n(\boldsymbol{\theta})\|^2} \geq 0$). The true parameter set is also the minimizer of $\mathscr{L}(\boldsymbol{\theta})$, hence satisfying risk consistency (i.e., Eq. 4). This result shows the minimization process in Eq. 3 converges to the true parameter dataset as the set of measurements tends to infinity if no model error is assumed.

Following the nomenclature proposed in [2], the estimation consistency of the model estimate is defined as:

$$\hat{\boldsymbol{\theta}}_n \xrightarrow{p} \hat{\boldsymbol{\theta}} \tag{13}$$

Estimation consistency ensures that the optimization process results in the true parameter set when the objective function is minimized. The prior discussion on risk consistency showed that the true parameter set is a minimizer of $\mathscr{L}_n$. Estimation consistency states that the true parameter set is the *only* global optimizer at the asymptotic limit. This can be satisfied if $C(1)$: the forward problem results in a unique set of displacements, $\mathbf{u}_i^{\text{sim}}(\boldsymbol{\theta})$, for a given set of parameters, $\boldsymbol{\theta}$, and $C(2)$ each set of displacements can only be generated by a unique set of parameters (identifiability condition). $C(1)$ requires strict convexity of the potential energy, Π_p, with respect to $\mathbf{u}^{\text{sim}}$ for each $\boldsymbol{\theta}$. The convexity of Π_p in terms of full-field displacement in linear elasticity is standard, for instance when $\mathbf{u}^{\text{sim}}$ represents all nodal displacement values of a finite element model [39]. The convexity of Π_p when $\mathbf{u}^{\text{sim}}$ is a subset of the nodal displacement vector that corresponds to measurement points is demonstrated in Appendix B. In Appendix C, $C(2)$ is studied for a one-dimensional composite specimen under known applied strain in which the spatial variation of the Young's modulus of the resin, $E_m(y; \boldsymbol{\theta})$, is characterized using the fiber centroid displacements as input. This study shows that a regular arrangement of fibers fails the identifiability condition regardless of the form of the spatial variation of the Young's modulus of the resin. In contrast, a random arrangement of fibers typically provides sufficient information to satisfy the identifiability condition. A general extension to a two-dimensional (2D) case is not straightforward, but it is reasonable to suppose that the identifiability condition is satisfied by considering sufficiently large datasets on specimens with randomly distributed fibers. This result suggests that the formulation proposed shows estimation consistency, Eq. 13. Therefore, provided a sufficiently large dataset is obtained, the true parameters can be identified despite the presence of random noise. The results obtained from several virtual characterizations reported in Section 3 support this supposition.

2.3 Optimization Algorithms

In the numerical studies performed in this section, two methods are employed to determine the parameters, $\hat{\boldsymbol{\theta}}_n$, that minimize Eq. 1: (1) the enumeration algorithm, and (2) sequential quadratic programming (SQP).

In the enumeration algorithm, the parameter space is sampled and the objective function is computed at every sampling point. This approach is often computationally prohibitive for cases when the number of parameters exceed two or three due to the exponential increase in the number of required sample points for a fixed discretization of each parameter. In the present work, the enumeration algorithm is employed to map the objective function and study its characteristics. To reduce the computational time the parameter space was discretized using a uniform grid that was finer near the optimum and coarser elsewhere. Additionally, the evaluations of the objective function at each grid-point were performed in parallel.

Gradient-based and evolutionary algorithms are well suited to solve optimization problems with several unknowns. In the present work, SQP is employed due to its suitability to solve constrained optimization problems [7], defined as bounds on the parameter space. All the parameters are normalized such that their value is within the range of $[0, 1]$. The Scipy Python package (version 1.91) [48] and method 'SLSQP' is employed as the SQP implementation [26]. The Jacobian matrix is evaluated using finite differences with a step size of 10^{-4}. In order to improve the likelihood of determining the global minimum, the multi-start method is employed, where optimizations are started with randomly selected initial conditions using stratified sampling of the parameter space [27]. The termination tolerance of the optimization is also set to 10^{-4}. The value for tolerance and finite difference step size were found to be a good compromise between accuracy and computational cost. The optimal solution is considered to be given by the parameters yielding the smallest objective function among all the optimizations.

3 Virtual characterization

In this section, the proposed approach is applied to a series of numerically-generated experimental data, henceforth designated synthetic experimental data, which is used in lieu of experimental data. Hence, each application of the approach is viewed as a virtual characterization. Since the true material properties used to generate the synthetic data are known, virtual characterizations are extremely valuable to understand and document the accuracy of the proposed approach. Using the enumeration algorithm, the following aspects of the inverse characterization approach proposed are investigated: (1) the identifiability condition and when it is fulfilled, (2) the effect of noise amplitude on the optimization results, and (3) the effect of the number of measurement points and microstructure via varying the fiber volume fraction.

3.1 Problem setup

In Fig. 2, the loading and boundary conditions used in the numerical simulations performed to generate the synthetic experimental data and evaluate the forward problem in the optimization algorithm are illustrated. 2D numerical models are subjected to 1% strain-controlled compressive loading under plane strain conditions. The random arrangement of fibers is created by a random sequential adsorption process [45]. The synthetic experimental data is generated by performing finite element simulations using assumed material properties and extracting displacements at the fiber centroids, mimicking the results from the FTM technique. As proposed in [11, 14], the FTM algorithm detects the 2D coordinates of fiber centroids in images captured within the transverse plane and measures the displacements of the fiber centroids by comparing the coordinates of the fiber centroids taken from images before and during loading. All finite element simulations were performed using the open-source package

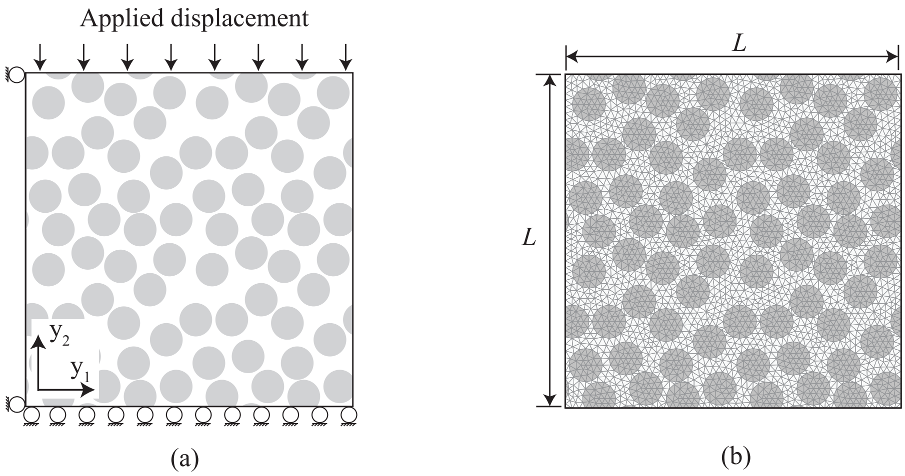

Fig. 2: Schematic illustration of the numerical specimen in the characterization examples. (a) Geometry, loading and boundary conditions. (b) Mesh discretization.

Table 1: Material properties of the composite constituents

Elastic properties of epoxy resin				
E_{int} [GPa]	α [μm^{-1}]	$\bar{E}_{\mathrm{m}}$ [GPa]	ν_m	
7.5426	0.23465	5.06	0.34	
Elastic properties of fiber				
E_1 [GPa]	E_2 [GPa]	G_{12} [GPa]	G_{13} [GPa]	ν_{31}
276	19.5	7.169	70	0.24

Calculix [15]. A sample discretization of the composite specimen, where linear tetrahedral elements are used to discretize the domain is shown in Fig. 2b.

The mechanical properties of the composite constituents are chosen to be similar to a typical graphite reinforced thermoset epoxy composite [4]. The fibers are modeled as transversely isotropic. All fibers are assumed to have the same, constant, Young's modulus. The Young's modulus of the isotropic resin is taken to be spatially variable. The resin Young's modulus associated with a spatial point, $E_{\mathrm{m}}(\mathbf{y})$, is assumed to be an exponential function of the distance, l, from the material point, $\mathbf{y}$, to the nearest fiber-resin interface:

$$E_{\mathrm{m}}(\mathbf{y}) = \left(E_{\mathrm{int}} - \bar{E}_{\mathrm{m}}\right) \exp\left(-\alpha l\right) + \bar{E}_{\mathrm{m}} \tag{14}$$

where E_{int} stands for the resin Young's modulus at the fiber-resin interface, α is a parameter that controls the variation of Young's modulus distribution, $\bar{E}_{\mathrm{m}}$ represents the Young's modulus at a large distance from the fiber-resin interface (i.e. $E_{\mathrm{m}} = \bar{E}_{\mathrm{m}}$, with $l \to \infty$) and its value can be considered to equal the Young's modulus of the neat resin. The aforementioned spatial variation is assumed based on the experiments gathered in [21], wherein in-situ measurements of the resin Young's modulus suggested an exponential relationship between the Young's modulus and the size of the resin pocket. Other forms for the spatial variation, requiring additional parameters, are discussed in Section 3.6. The experimental measurements for E_{int}, $\bar{E}_{\mathrm{m}}$ and α obtained in Ref. [21] are employed for generating synthetic measurement data and listed in Table 1 along with the

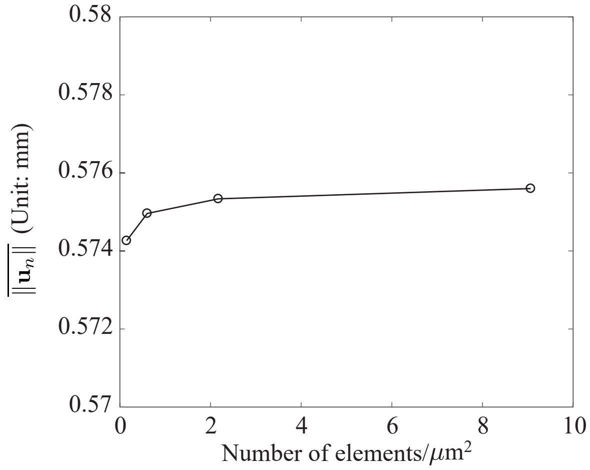

Fig. 3: Average fiber centroid displacement magnitude vs. mesh size density.

Poisson ratio, ν_m, and the Young's modulus of the fibers. The results of the finite element simulation assuming the properties in Table 1 are used as the synthetic experimental data.

The synthetic experimental data is subsequently post-processed to extract the displacements at the nodes positioned at fiber centroids. The mesh density used in the finite element simulations is checked to minimize the finite element model error. As shown in Fig. 3, the discrepancy of average fiber centroid displacement compared between the coarsest and finest mesh is only 0.2%. A mesh size density of 0.6 elements/μm^2 is employed throughout this work.

In the present work, the displacement measurements are polluted with randomly generated Gaussian noise, which can be traced back to the image resolution used in the FTM approach [11]. To obtain an estimate for the expected relationship between noise amplitude and image resolution, as well as the expected noise amplitude, FTM was applied to track the fiber centroid displacements using images of a deformed and reference numerical model obtained with three levels of image resolution: 1 pixel/μm, 10.7 pixels/μm and 32.5 pixels/μm. As shown in Fig. 4, the standard deviations of the absolute error for each displacement component range from 0.0025 μm to 0.2 μm. The standard deviations of u_{y_1} and u_{y_2} are approximately the same for both 32.5 pixels/μm and 10.75 pixels/μm. In the following virtual characterizations, the standard deviation of the assumed Gaussian noise is considered to range from 0 μm to 0.1 μm and is assumed to be the same for both u_{y_1} and u_{y_2}, as suggested by the results obtained for 32.5 pixels/μm and 10.75 pixels/μm, to satisfy the assumption of standard deviation that: $\mathbb{E}(\epsilon_{y_1}) = \mathbb{E}(\epsilon_{y_2}) = \sigma_\epsilon^2$.

3.2 Identifiability assessment

In this section, the identifiability condition using 2D numerical specimens is studied for two unknown parameters (i.e. $\boldsymbol{\theta} = \{E_{\text{int}}, \alpha\}$). Identifiability is checked by directly plotting the objective function landscape probed using the enumeration algorithm. The spacing for the grids is set at $\Delta E_{\text{int}} = 0.2$ MPa and $\Delta\alpha = 0.02$, while the finer grid spacing near the optimum is established with $\Delta E_{\text{int}} = 0.02$ MPa and $\Delta\alpha = 0.005$. Three specimens were created with different fiber arrangements as shown in Fig. 5, where the domain size is $L = 100\mu$m and the fiber radius is 5μm. The specimens include a regular grid of fibers (Fig. 5a), a regular grid with a resin rich region (Fig. 5b), and a specimen with random fiber arrangement (Fig. 5c). The corresponding fiber volume fractions for these arrangements are 50.27%, 43.98%, and 53.41%, respectively. No measurement noise is added to fiber centroid displacements. The contours of the objective function (denoted by percentage value) generated at the grid points in the parameter space are shown in Figs. 5d–f. The contour is displayed in the parameter space scaled by

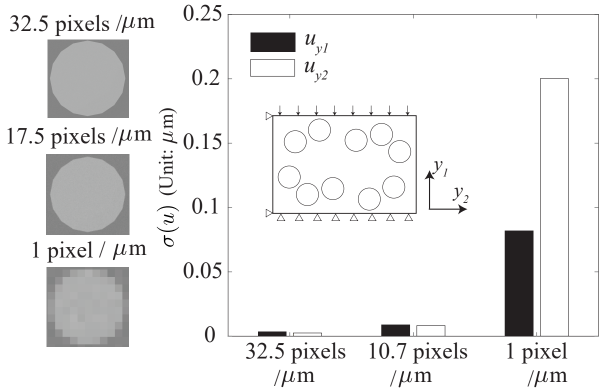

Fig. 4: Standard deviations of displacement components for different image resolutions. The numerical specimen is shown as an inset in the figure.

the relative error:

$$\epsilon_{\boldsymbol{\theta}}^{\text{rel}} = \left| \frac{\hat{\theta} - \theta_{\text{true}}}{\theta_{\text{true}}} \right| \tag{15}$$

The zero point (denoted by a red circle) in the contour plot represents the true value of these parameters. As shown in Fig. 5d, the specimen with uniform resin pocket size (Fig. 5a) has multiple minima since the contour lines near the true value are not closed. The objective function along a line segment that passes through the true parameter set is plotted below the contour plot. As can be observed in Fig. 5d, the objective function is zero for multiple parameter sets, including, but not limited to, the parameter set corresponding to the true values of the parameters. Therefore, in this case, the parameters are not uniquely identifiable and, hence, the optimization problem is not strictly convex. The objective function landscapes for the microstructure with two or more distinct resin pocket sizes (see Fig. 5b and 5c) have closed contour lines near the true value. The objective function along the line segment that passes to the true parameter set is zero only when the parameter set equals the true value of the parameters. The identifiability condition is therefore satisfied, indicating convexity of the optimization problem. These results suggest that the identifiability condition is affected by the fiber arrangement when using fiber centroid displacements to infer spatially distributed resin properties. The relationship between fiber and resin geometric arrangement and the identifiability condition is further studied in the Appendix C via a 1-dimensional (1D) problem. The 2D results reported, as well as the insight obtained through the 1D study in Appendix C, indicate that, provided the number of different resin pocket sizes is larger than the number of material parameters that need to be determined, the identifiability condition is met. Hence, given the random nature of typical fiber arrangements, a complex spatial variation of material properties (with complexity judged by number of parameters) can be assumed without compromising the identifiability condition.

3.3 Effect of noise

A specimen of size $L = 200\mu$m with a random arrangement of fibers (radius of 5μm) is employed. The fiber volume fraction is set to 55% and there are 280 fibers in total within the specimen. Each displacement component in the fiber centroid displacement measurements is assumed to be corrupted with independent Gaussian noise with zero mean and standard deviation designated by σ_ϵ. To study the variability of the virtual characterization results in the presence of noise, the virtual characterization is repeated 100 times using different synthetic experimental data each time. Each synthetic dataset is created by adding different noise realizations, but with the same standard deviation, to a noise free dataset. The effect of the noise amplitude is studied by adjusting the value of the standard deviation which takes

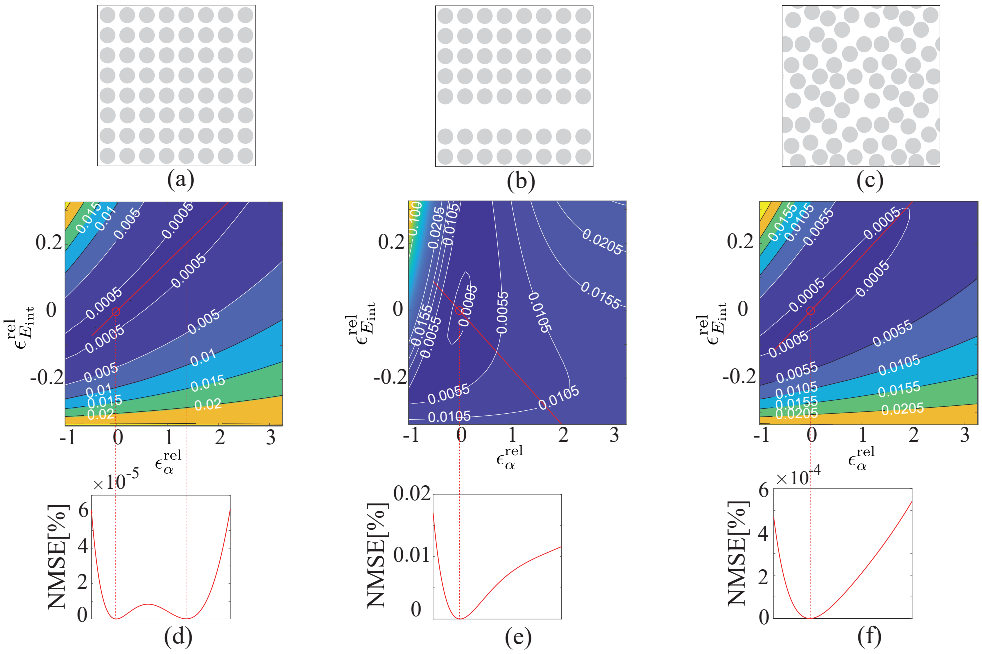

Fig. 5: The specimen with (a) a regular grid of fibers, (b) a grid of a resin rich region, and (c) random fiber arrangement. (d), (e), and (f) are the objective function landscapes corresponding to (a), (b), and (c), respectively. In the first row the objective function value as a function of the two parameters, E_{int} and α is illustrated. In the second row the value of objective function along the red lines denoted in the first-row contours is displayed.

values from $\sigma_\epsilon = 0$ μm to $\sigma_\epsilon = 0.1$ μm in increments of 0.01 μm. The enumeration algorithm is employed for the optimization. In this exercise, the virtual characterization aims to determine the Young's modulus, E_{int}, and spatial variance parameter, α, in Eq. 14, and assumes all other material properties are known. The grid spacing is configured to match that of Section 3.2, and it is also utilized for the enumeration algorithm examples in the subsequent sections. In Fig. 6a, the statistics of the error of displacement prediction relative to the true displacement field ($\mathscr{L}_{\text{true}} := \sum_{i=1}^{n} \|\mathbf{u}_i - \mathbf{u}_i^{\text{sim}}\|^2 / \sum_{i=1}^{n} \|\mathbf{u}_i\|^2$) are reported as a function of the noise amplitude. The mean value (denoted by a circle) and the standard deviation (denoted by a whisker) of true prediction error are amplified when the amplitude of the noise increases. The mean values and the standard deviations of the relative errors in $\{E_{\text{int}}, \alpha\}$ are shown in Figs. 6b and c. The errors in identifying E_{int} and α reach $18.8\% \pm 12\%$ and $143.8\% \pm 100\%$, respectively, at the highest noise amplitude considered. The overall error in the identification of resin Young's modulus is measured by the maximum relative error within the modulus distribution (named maximum Young's modulus error herein), expressed by $\epsilon^{\text{rel}}_{\max} = \max_{\mathbf{y}} |(\hat{E}_{\text{m}}(\mathbf{y}) - E_{\text{m}}(\mathbf{y}))|/E_{\text{m}}(\mathbf{y})$, where $E_{\text{m}}(\mathbf{y})$ is the true distribution. As shown in Fig. 6d, the Young's modulus error reaches a maximum of $28\% \pm 13.7\%$ at the highest noise amplitude, despite a significantly higher error in α being registered at the same noise amplitude.

3.4 Alleviating the effects of measurement noise

The corrupting effect of noise can be alleviated by increasing the number of sampling points for measurement as discussed in Section 2.2. In the context of using fiber centroids for measurements, enlarging the specimen size, hence increasing the number of fibers, n_{f}, or performing n_{exp} experiments can increase the sampling points for the measurement, n, given by $n = n_{\text{exp}} n_{\text{f}}$.

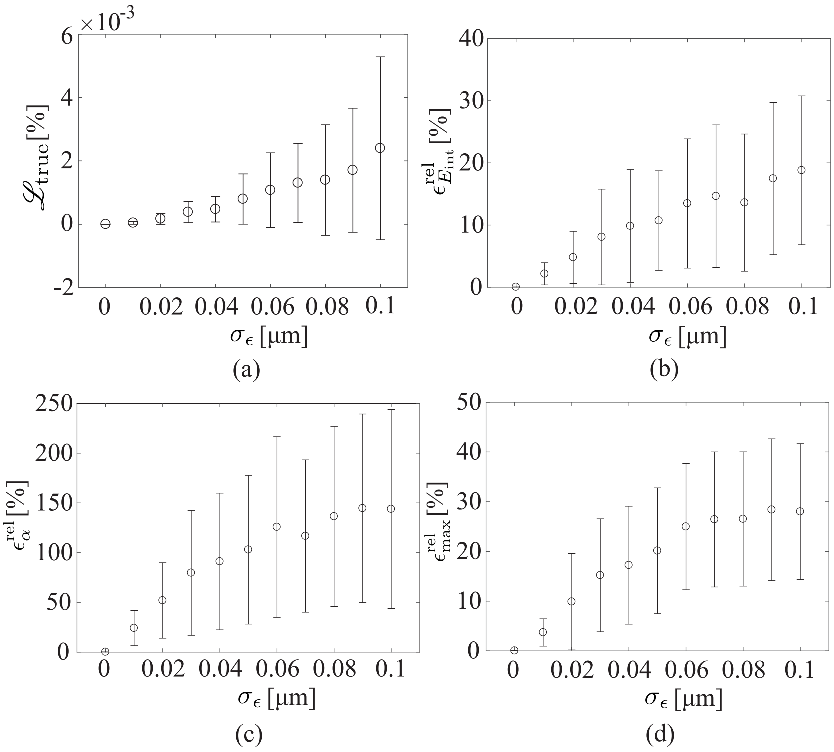

Fig. 6: The mean value (circle) and standard deviation (whisker) of (a) displacement prediction error, (b) E_{int}, (c) α, (d) maximum relative error in Young's modulus within the distribution, for the characterizations using a 200μm specimen with different noise levels represented by the standard deviation σ_ϵ.

Those points are named "measurement points" for brevity. In the following virtual characterizations, three specimens with fiber volume fraction of 55% and length (i.e. L in Fig. 2) of 200 μm, 500 μm, and 1 mm are employed. The total number of fibers are 280, 1,750, and 7,000 for $L = 200$ microns, 500 microns, and 1 mm, respectively. In order to increase the number of measurement points, the same specimens were unloaded and reloaded elastically $1, 2, 5, 10, 20$ times. The virtual characterizations are repeated for 100 times for each specimen loaded n_{exp} times. The measurement error is introduced independently for each virtual characterization with standard deviation of $\sigma_e = 0.1$ μm.

The mean values and ranges of displacement prediction error obtained by the enumeration algorithm are shown in Figs. 7a through 7c for each specimen as the number of measurement points, n, increases. The prediction error reveals less variance with increasing n and the error introduced by the measurement noise is reduced.

In Fig. 8, the mean value and standard deviation of the relative error of E_{int}, α, and the maximum relative error in Young's modulus whithin the distribution are depicted as a function of the measurement points. The results for each specimen size are discriminated by different colors and markers. For a fixed-sized specimen, a monotonically decreasing trend of bias and variance in the identified parameters with increase in the number of measurement points can be observed. The number of measurements points is increased by performing more experiments on the same specimen. The maximum error in Young's modulus reduces from 28% $\pm$ 13.7% (200 μm specimen loaded a single time) to 1.48% $\pm$ 1.13% (1 mm specimen loaded 10 times), and 1.12% $\pm$ 0.82% (1 mm specimen loaded 20 times).

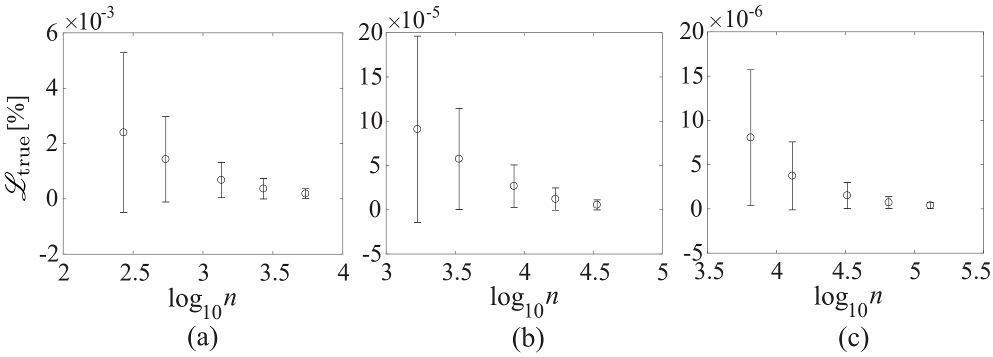

Fig. 7: The mean value (circle) and standard deviation (whisker) of the displacement prediction error for (a) 200 μm, (b) 500 μm and (c) 1 mm specimen unloaded and reloaded 1, 2, 5, 10 and 20 times with noise amplitude of $\sigma_\epsilon = 0.1\mu$m. n stands for total number of measurement points.

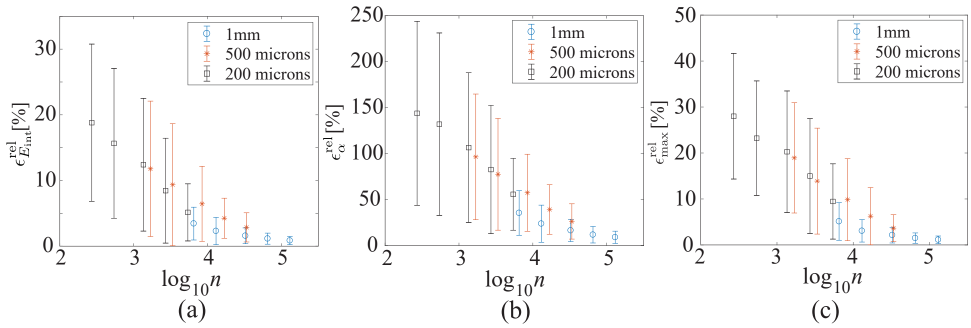

Fig. 8: The mean value (marker) and standard deviation (whisker) of the relative error of (a) E_{int}, (b) α, and (c) maximum Young's modulus within the distribution, for the characterizations of 200 μm, 500 μm, and 1 mm specimens unloaded and reloaded 1, 2, 5, 10, 20 times with noise amplitude of $\sigma_\epsilon = 0.1\mu$m.

In Fig. 9a, the characterized Young's modulus variation for 100 inverse characterizations are plotted as a function of the distance from the nearest fiber, l, based on the measurements of a 1 mm specimen loaded 20 times (denoted by gray lines) and compared to the true value (denoted by black lines). Among 100 inverse characterizations, most characterization results deviate from the reference distribution at $l = 0$ μm (i.e., at the interface) and beyond 1 μm. The errors are at their lowest around $l = 1$ μm. The contours of the relative error in Young's modulus are illustrated in Fig. 9b, which confirms the trend that the higher discrepancies occur at the fiber/resin interface (yellow region indicated by positve error) and the center of the resin pocket (blue region indicated by negative error). This trend is attributed to the observation that (a) the actual resin Young's modulus distribution in a specimen is bounded by the proximity of the fibers; and (b) the upper bound of the resin Young's modulus in the finite element computation is dictated by the distance between the fiber-resin interface and the closest integration points in the resin. Regarding the latter, refining the mesh near the interfaces would allow more measurement points for interface Young's modulus (E_{int}) and hence its identification. Regarding the former, the histogram of distances between each integration point in the resin and the nearest fiber in the mesh is shown in Fig. 9a. Most of the integration points in the resin phase have the nearest fiber distance ranging from $0\mu\text{m} < l < 5\mu\text{m}$, the range where the error in Young's modulus variation reaches minimum. The results in Fig. 9a suggest that the magnitude of the error in the estimated modulus (for each point at a distance l from the nearest fiber) is affected by the range of distances between fibers within the microstructure.

3.5 Effect of fiber volume fraction on characterization error

The fiber volume fraction affects property identification in two ways. For a fixed-sized specimen, a reduction in fiber volume fraction implies a reduction in the number of measurement points (assuming data collection is restricted to fiber centroid displacements) and hence adversely affects the identification process. However, a relatively low fiber volume also implies a larger fiber-to-fiber distance in the specimen and hence a more uniform sampling of resin modulus variation. We consider fiber volume fractions 15%, 30%, 42%, and 55% in 500 μm specimens. Each specimen is subjected to 1, 2, 5, 10, and 20 load-unload cycles. Virtual characterizations are repeated 100 times using noisy synthetic experimental data, generated as described in Section 3.3, with an assumed noise amplitude of $\sigma_e = 0.1\mu$m. In Fig. 10, the mean value and standard deviation of the characterization error for each volume fraction is reported as a function of number of measurement points. The reducing trend in the error associated with E_{int} is apparent. Decreasing volume fraction also lowers the estimation error of the spatial variation term, α. This is because the specimen with lower volume fraction has larger sizes of resin pockets amid the fibers resulting in a more even sampling of the spatial variation of the resin modulus. Hence, the specimen with the lower volume fraction exhibits a higher sensitivity of displacement response to the changes in the spatial variation term α and therefore the effect of the noise diminishes, despite the smaller number of measurement points. The characterization error in the examples with a relative higher volume fraction of 55% is less susceptible to the impact of reducing the size of the resin pocket. In this scenario, the increased number of measurement points (i.e. number of embedded fibers) plays a more significant role, resulting in a slightly lower characterization error compared to the 42% cases.

3.6 Increasing the parameter set size

In this section, larger sets of parameters describing a more complex spatial variation of resin properties are identified using the SQP optimization approach described in Section 2.3. A specimen of size $L = 500\mu$m and 42% fiber volume fraction (55 fibers) is employed. The specimen is subjected to 20 load-unload cycles. The synthetic datasets used are assumed to be polluted by random noise with $\sigma_e = 0.01\mu$m, corresponding to the image resolution of 10.7 pixels per micron in Fig. 4.

The resin modulus is taken to vary at two scales. The variation at the lower scale is assumed to be adequately represented by the exponential form of Eq. 14. To capture the variation at a coarser scale, a harmonic form is added to Eq. 14 yielding:

$$E_{\text{m}}(\mathbf{y}) = \left(E_{\text{int}} - \bar{E}_{\text{m}}\right)\exp\left(-\alpha l\right) + \bar{E}_{\text{m}} + A\sin\left(\frac{2\pi y_1}{\lambda_{y_1}}\right)\sin\left(\frac{2\pi y_2}{\lambda_{y_2}}\right) \tag{16}$$

in which λ_{y_1} and λ_{y_2} are the wave lengths of harmonic variations along the y_1 and y_2 directions and A is the amplitude of harmonic variation. The harmonic form chosen is not physically motivated and can be revisited as needed.

In the following virtual characterizations, the number of unknown model parameters, $\boldsymbol{\theta}$, is progressively increased. The true values, $\hat{\boldsymbol{\theta}}$, are listed in Table 2 for reference. The Poisson's ratio of the resin is assumed to be unknown for all the examples. In cases 2–4, the remote resin modulus, $\bar{E}_{\text{m}}$, is also considered as an unknown parameter in addition to E_{int} and α. The harmonic variation of Young's modulus in Eq. 16 is included in cases 3 and 4. Case 3 assumes that the wavelength of the variation is identical in two spatial directions ($\lambda_{y1} = \lambda_{y2} = 200\mu$m). In case 4, the harmonic wavelengths are assumed to be different: $\lambda_{y1} = 200\mu$m, $\lambda_{y2} = 300\mu$m.

The characterization results and error values are displayed in Table 2. The error in the Poisson's ratio is almost negligible in all cases. This is because the Poisson's ratio is only related to the ratio of normal strains at two directions, and the overall vertical strain is relatively fixed since

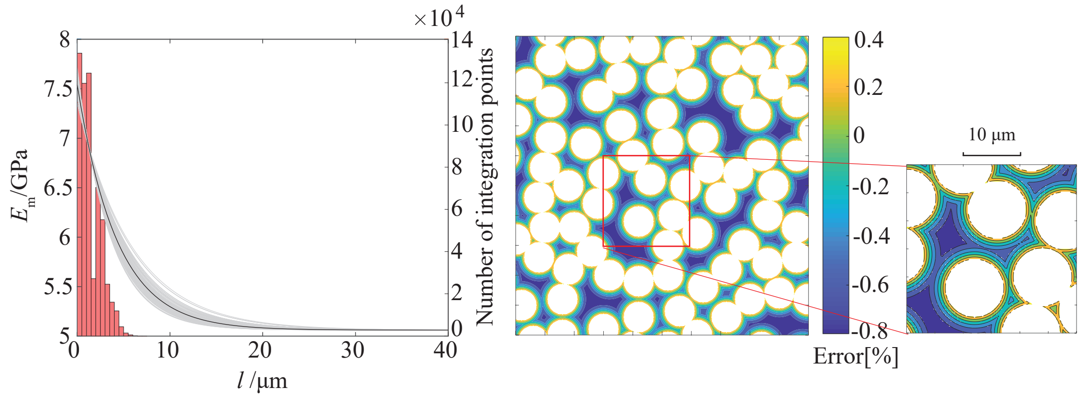

(a) (b)

Fig. 9: (a) The estimated resin Young's modulus variation (gray lines) vs. true distribution (black line), and the histogram of integration points number in the resin phase for various distances from the nearest fiber l, (b) the contour of relative error of the resin Young's modulus: $(\hat{E}_\mathrm{m}(\mathbf{y}) - E_\mathrm{m}(\mathbf{y}))/E_\mathrm{m}(\mathbf{y})$ over the central inner $100\mu m \times 100\mu m$ region for one of the estimation, based on the measurement 1 mm specimen loaded 20 times.

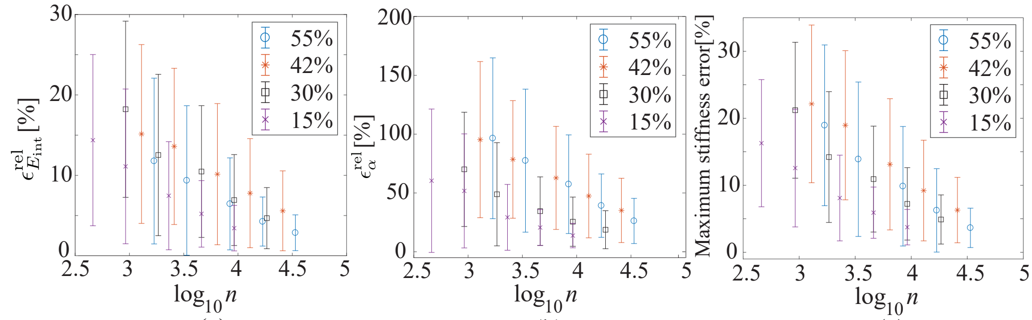

(a) (b) (c)

Fig. 10: The mean value (marker) and standard deviation (whisker) of the relative error of (a) E_{int}, (b) α, and (c) maximum Young's modulus within the distribution, for characterizations of a 500 μm specimen with 15%, 30%, 42%, and 55% fiber volume fraction loaded 1, 2, 5, 10, and 20 times with the highest noise level of $\sigma_\epsilon = 0.1\mu m$.

the specimen is under constant displacement-controlled compressive loading. For modulus characterization, case 2 results indicate that the current characterization approach identifies the neat resin properties with good accuracy in addition to the interface modulus and the spatial variation parameter. In cases 3 and 4, the characterization is performed for 6 and 7 parameters, respectively. The characterizations for large-wavelength harmonic variation are accurate for both the amplitude, A, and the wavelengths $(\lambda_{y1}, \lambda_{y2})$, while the accuracy for fine-scale exponential variation is lower compared to the cases 1 and 2. The lower accuracy is attributed to the increased difficulty in finding the global minimum in a relatively high dimensional space using a gradient based optimization approach, for modulus properties varying at two spatial scales. Approaches to improve accuracy in this case may include increasing the number of optimization starting points, at the expense of additional computation time, investigating strategies to increase the accuracy in the Jacobian matrix calculation and revisiting the selection of tolerance for termination of the optimization. As shown in Fig. 11, the larger relative

Table 2: Reference parameters of epoxy resin properties and the SQP characterization results

		E_{int} [GPa]	α	$\bar{E}_{\text{m}}$ [GPa]	A [GPa]	λ_{y1} [μm]	λ_{y2} [μm]	ν_m
Case 1	$\hat{\boldsymbol{\theta}}$	7.5426	-0.23465	/	/	/	/	0.34
	SQP	7.49	-0.217	/	/	/	/	0.3399
	Error	-0.68%	-7%	/	/	/	/	$< 0.1\%$
Case 2	$\hat{\boldsymbol{\theta}}$	7.5426	-0.23465	5.06	/	/	/	0.34
	SQP	7.49	-0.22	5.04	/	/	/	0.3399
	Error	-0.7%	-5%	-0.32%	/	/	/	$< 0.1\%$
Case 3	$\hat{\boldsymbol{\theta}}$	7.5426	-0.23465	5.06	2	200	/	0.34
	SQP	7.88	-0.392	5.65	2.03	200	/	0.339
	Error	4.48%	-69%	11%	1.67%	$< 0.1\%$	/	$< 0.1\%$
Case 4	$\hat{\boldsymbol{\theta}}$	7.5426	-0.23465	5.06	2	200	300	0.34
	SQP	8.228	-0.6	5.86	2.02	200	300	0.339
	Error	9%	-155%	15.8%	1.09%	$< 0.1\%$	$< 0.1\%$	$< 0.1\%$

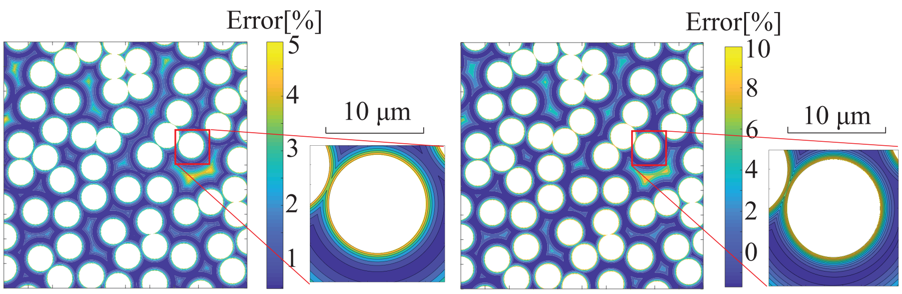

(a) (b)

Fig. 11: The contours of the relative error of the resin modulus over the central $100\mu m \times 100\mu m$ region within the 500 μm specimen, as well as refined contours for one of the fibers and its surrounding, obtained for the harmonic variation characterization of (a) $\boldsymbol{\theta} = \{E_{\text{int}}, \alpha, \bar{E}_{\text{m}}, \nu_{\text{m}}, A, \lambda_{y1}\}$, (b) $\boldsymbol{\theta} = \{E_{\text{int}}, \alpha, \bar{E}_{\text{m}}, \nu_{\text{m}}, A, \lambda_{y1}, \lambda_{y2}\}$

.

errors of resin modulus are at the fiber-resin interface and larger resin pockets. The largest value is very similar to the error of interface modulus E_{int}. The larger error in α is attributed to the dominating effect of the large-scale harmonic variation of modulus over the exponential fine-scale variation which results in displacement measurements that are less sensitive to α.

4 Conclusion

This manuscript developed an inverse characterization approach for identifying spatially heterogeneous in-situ elastic properties of composite materials based on microscopic image-based experimental measurements. Particular attention is given to the effect of random noise polluting the input data. To ensure the inverse characterization problem was formulated such that the correct solution can be obtained despite the presence of measurement noise, concepts of statistical inference theory were used to analyze the objective function and the forward problem and guide their formulation. This analysis suggests that the true material properties can be identified provided a sufficient number of measurement points are obtained (i.e., the inverse problem is estimation consistent). The estimation consistency of the approach is further examined and documented through several virtual characterizations. The virtual characterizations use numerically generated data, named synthetic data, in lieu of experimental data. The synthetic data consists of noisy fiber centroid displacements (measurement points), mimicking the measurements obtained with fiber template matching extracted from simulations performed with known (true) material properties. In the virtual characterizations, the synthetic data is used to determine the parameters of assumed functional forms defining the spatial variation of the properties of the material, which can be compared to the true material properties. The results show that the effect of measurement noise is progressively reduced by increasing the number of measurement points, which can be achieved by increasing the specimen size (and hence the number of fibers tracked) or by performing multiple experiments on a single specimen, or multiple specimens, as long as they exhibit a similar spatial variation in properties. Furthermore, characterization accuracy could also be improved by specimen design, where the specimen domain is tailored to include factors (e.g., resin pockets, functional gradients of fiber volume fraction, etc.) that provide sufficient sampling to identify the parameters for describing the spatial variation of the properties, such as resin modulus. We note that such an approach could be restricted by manufacturing constraints. Using SQP, a larger set of parameters, representing variability at different scales, was identified suggesting that the proposed inverse modeling framework can be further generalized if required. The accuracy of the identified parameters in such cases are naturally influenced by the efficacy of the optimization tool and the size and richness of the dataset used.

Future work may include the study of the model error (or bias) which can be caused by numerical error or the image noise with non-zero mean value. These are considered outside the scope of this initial study. In this context, a Bayesian approach to the problem may be worth pursuing as it could enable one to quantify uncertainty in the parameter evaluation while considering the effect of both measurement noise and model error. Given the relatively large number of model evaluations typically required in a Bayesian framework, such an approach may also require the use (and development) of a micro-scale surrogate model.

Acknowledgments. The authors gratefully acknowledge financial support provided through the NASA Langley Research Center IRAD program (with Subaward No. 80LARC17C0004 to Vanderbilt University by the National Institute of Aerospace).

Appendix A The conditions of objective function minimization with noise

Assume that the objective function $\mathscr{L}_n$ in Eq. 7 under noise is minimized at $\hat{\boldsymbol{\theta}} = \{\hat{\theta}_1, \hat{\theta}_2 \ldots \hat{\theta}_m\}$ and it is satisfied when $\partial \mathscr{L}/\partial \boldsymbol{\theta} = \mathbf{0}$. Using the chain rule, the following equation can be derived by incorporating the noise term in the measurements (see Eq. 6):

$$\left.\frac{\partial \mathbf{u}^{\mathrm{sim}}}{\partial \boldsymbol{\theta}}\right|_{\hat{\boldsymbol{\theta}}} \cdot \left(\mathbf{u}^{\mathrm{sim}} - \mathbf{u} - \boldsymbol{\epsilon}\right) = 0 \tag{A1}$$

Consider the following three conditions:

1. $\left.\partial \mathbf{u}^{\mathrm{sim}}/\partial \boldsymbol{\theta}\right|_{\hat{\boldsymbol{\theta}}} = \mathbf{0}$. According to mean value theorem [36], there exists different parameter vectors $\boldsymbol{\theta}_a = \{\theta_{a1}, \theta_{a2} \ldots \theta_{am}\}$ and $\boldsymbol{\theta}_b = \{\theta_{b1}, \theta_{b2} \ldots \theta_{bm}\}$ satisfying $\hat{\theta}_1 \in (\theta_{a1}, \theta_{b1})$, $\hat{\theta}_2 \in (\theta_{a2}, \theta_{b2}) \ldots \hat{\theta}_m \in (\theta_{am}, \theta_{bm})$, such that:

$$\|\mathbf{u}^{\mathrm{sim}}(\boldsymbol{\theta}_a) - \mathbf{u}^{\mathrm{sim}}(\boldsymbol{\theta}_b)\| \leq \left\| \left.\frac{\partial \mathbf{u}^{\mathrm{sim}}}{\partial \boldsymbol{\theta}}\right|_{\hat{\boldsymbol{\theta}}} \right\| \|\boldsymbol{\theta}_a - \boldsymbol{\theta}_b\| = 0 \tag{A2}$$

Then we can obtain $\mathbf{u}^{\mathrm{sim}}(\boldsymbol{\theta}_1) = \mathbf{u}^{\mathrm{sim}}(\boldsymbol{\theta}_2)$ since $\|\cdot\| \geq 0$. In this case, the identifiability condition (i.e. $\mathbf{u}^{\mathrm{sim}}(\boldsymbol{\theta}_1) = \mathbf{u}^{\mathrm{sim}}(\boldsymbol{\theta}_2)$ only if $\boldsymbol{\theta}_1 = \boldsymbol{\theta}_2$) is not satisfied. The detailed discussion about the identifiability condition is provided in Appendix C.

2. $\mathbf{u}^{\text{sim}} - \mathbf{u} - \boldsymbol{\epsilon} = \mathbf{u}^{\text{sim}} - \mathbf{u}^{\text{mes}} = \mathbf{0}$. Typically, this condition is not satisfied, because $\mathbf{u}^{\text{sim}}$ follows the equilibrium equation, whereas, $\mathbf{u}^{\text{mes}}$ does not satisfy equilibrium due to the presence of noise term.

3. $\partial\mathbf{u}^{\text{sim}}/\partial\boldsymbol{\theta} \neq \mathbf{0}$, $\mathbf{u}^{\text{sim}} - \mathbf{u} - \boldsymbol{\epsilon} \neq \mathbf{0}$. If we assume that the objective function is minimized at the true displacement $\mathbf{u}$ (i.e., $\mathbf{u} = \mathbf{u}^{\text{sim}}$), there is:

$$\left.\frac{\partial \mathbf{u}^{\text{sim}}}{\partial \boldsymbol{\theta}}\right|_{\boldsymbol{\theta}} \cdot \boldsymbol{\epsilon} = 0 \tag{A3}$$

Equation A3 is not necessarily satisfied as $\boldsymbol{\epsilon}$ is a random variable. In this case, the true displacements do not minimize the objective function with noise, therefore the parameter vector $\hat{\boldsymbol{\theta}}$ identified by the optimization does not contain the true parameters.

Appendix B Strict convexity of the forward problem: subset of displacements vs. full displacement field

Using the finite element method, the potential energy in terms of a nodal displacement vector $\mathbf{U}$, the stifness matrix $\mathbf{K}$ and force vector $\mathbf{F}$ is expressed as [39]:

$$\Pi_p = \frac{1}{2}\mathbf{U}^T\mathbf{K}\mathbf{U} - \mathbf{U}^T\mathbf{F} \tag{B4}$$

Consider that $\mathbf{u}_{\text{sim}}$ consists of a subset of the nodal displacements and they do not overlapped with the boundaries with enforced displacements. Aggregating the displacement at the measurement points, Eq. B4 can be rewritten as:

$$\begin{aligned}\Pi_p =& \frac{1}{2}\left[(\mathbf{u}_{\text{sim}})^T, (\mathbf{u}_{\text{r}})^T\right]\begin{bmatrix}\mathbf{K}_{\text{ss}} & \mathbf{K}_{\text{sr}}\\ \mathbf{K}_{\text{rs}} & \mathbf{K}_{\text{rr}}\end{bmatrix}\begin{bmatrix}\mathbf{u}_{\text{sim}}\\ \mathbf{u}_{\text{r}}\end{bmatrix}\\ &- \left[(\mathbf{F}_{\text{s}})^T, (\mathbf{F}_{\text{r}})^T\right]\begin{bmatrix}\mathbf{u}_{\text{sim}}\\ \mathbf{u}_{\text{r}}\end{bmatrix}\end{aligned} \tag{B5}$$

where, $\mathbf{u}_{\text{r}}$ collects the nodal displacements at locations other than the measurement points, $\mathbf{K}_{\text{ss}}$, $\mathbf{K}_{\text{sr}}$, $\mathbf{K}_{\text{rs}}$ and $\mathbf{K}_{\text{rr}}$ are stiffness submatrices, $\mathbf{F}_{\text{s}}$ and $\mathbf{F}_{\text{r}}$ are force subvectors after reordering.

Let $\mathbf{U}^* = [\mathbf{u}^*_{\text{sim}}, \mathbf{u}^*_{\text{r}}]^T$ denote a nodal displacement vector. The principle of minimum energy $\partial\Pi_p/\partial\mathbf{U}|_{\mathbf{U}=\mathbf{U}^*} = 0$ results in:

$$\mathbf{K}_{\text{ss}}\mathbf{u}^*_{\text{sim}} + \mathbf{K}_{\text{sr}}\mathbf{u}^*_{\text{r}} = \mathbf{F}_{\text{s}} \tag{B6}$$
$$\mathbf{K}_{\text{rs}}\mathbf{u}^*_{\text{sim}} + \mathbf{K}_{\text{rr}}\mathbf{u}^*_{\text{r}} = \mathbf{F}_{\text{r}} \tag{B7}$$

Consider another state of nodal displacements $\mathbf{U}^{**} = [\mathbf{u}^{**}_{\text{sim}}, \mathbf{u}^*_{\text{r}}]^T$, in which the nodal displacements at the measurement points $\mathbf{u}^{**}_{\text{sim}}$ are different from $\mathbf{u}^*_{\text{sim}}$. The strict convexity of potential energy with respect to the subset of nodal displacement $\mathbf{u}_{\text{sim}}$ leads to the following inequality [8]:

$$\Pi_p\left(\mathbf{U}^{**}\right) - \Pi_p\left(\mathbf{U}^{*}\right) - \frac{\partial\Pi_p}{\partial\mathbf{u}_{\text{sim}}}\Delta\mathbf{u}_{\text{sim}} > 0 \tag{B8}$$

where $\Delta\mathbf{u}_{\text{sim}} = \mathbf{u}^{**}_{\text{sim}} - \mathbf{u}^*_{\text{sim}}$. Substituting Eqs. B5 and B6 in Eq. B8 results in:

$$[\Delta\mathbf{u}_{\text{sim}}]^T[\mathbf{K}_{\text{ss}}][\Delta\mathbf{u}_{\text{sim}}] > 0 \tag{B9}$$

Therefore, strict convexity is satisfied only if $[\mathbf{K}_{\text{ss}}]$ is positive definite. It is well-known that the stiffness matrix $[\mathbf{K}]$ is already positive definite according to the energy minimization principal. For arbitrary non-zero vector $\mathbf{x} \in \mathbb{R}^N \setminus \{\mathbf{0}\}$, there is $\mathbf{x}^T\mathbf{K}\mathbf{x} > 0$. $[\mathbf{K}_{\text{ss}}]$ can be proved to be positive definite by assuming another arbitrary non-zero vector $\mathbf{v} \in \mathbb{R}^n \setminus \{\mathbf{0}\}$ and $\mathbf{x}^* = [\mathbf{v}; \mathbf{0}]$, which holds:

$$\begin{aligned}\mathbf{x}^{*T}\mathbf{K}\mathbf{x}^* &= \left[\mathbf{v}^T, \mathbf{0}^T\right]\begin{bmatrix}\mathbf{K}_{\text{ss}} & \mathbf{K}_{\text{sr}}\\ \mathbf{K}_{\text{rs}} & \mathbf{K}_{\text{rr}}\end{bmatrix}\begin{bmatrix}\mathbf{v}\\ \mathbf{0}\end{bmatrix}\\ &= [\mathbf{v}^T][\mathbf{K}_{\text{ss}}][\mathbf{v}] > 0\end{aligned} \tag{B10}$$

Appendix C Discussion of identifiability condition in 1D composite specimen

Consider a composite bar of length L (See Fig. C1) under the displacement loading U. There are n "fibers" with length r and Young's modulus of E_f. The "matrix" Young's modulus E_m is assumed to vary spatially with the distance (l) from the nearest fiber interface. The measured fiber centroid displacements $u_{(i)}, i = 1, 2, \ldots n$ are considered to be the inputs of the optimization problem that aims to characterize the parameter $\boldsymbol{\theta}$, which defines the spatial variation of the resin modulus. It is straightforward to obtain an anlytical expression for the fiber centroid displacements $u_{(i)}, i = 1, 2 \ldots n$:

$$u_{(i)} = \frac{\left[\sum_{j=0}^{i-1} \bar{C}_{m_j} l_j E_f + (2i-1) r\right] U}{\sum_{j=0}^{n+1} \bar{C}_{m_j} l_j E_f + 2nr} \tag{C11}$$

where $\bar{C}_{m_i}$ stands for the average compliance of the resin part between $i-1^{th}$ and i^{th} fiber, $\bar{C}_{m_0}$ for the resin part between left specimen boundary and the leftmost fiber, $\bar{C}_{m_{n+1}}$ for the resin part between right boundary and rightmost fiber. In terms of resin length, l_i, the average compliance is expressed as:

$$\bar{C}_{mi} = \begin{cases} \dfrac{1}{l_i} \displaystyle\int_0^{l_i} \dfrac{\mathrm{d}x}{E_m\left(l; \boldsymbol{\theta}\right)}; & i = 0, n \\ \dfrac{2}{l_i} \displaystyle\int_0^{l_i/2} \dfrac{\mathrm{d}x}{E_m\left(l; \boldsymbol{\theta}\right)}; & i = 1, 2 \ldots n-1 \end{cases} \tag{C12}$$

Let us assume that the same displacement measurements $(\hat{u}_{(i)}, i = 1, 2 \ldots n)$ can be obtained with a different set of constitutive parameters, $\hat{\boldsymbol{\theta}}$:

$$\hat{u}_{(i)} = \frac{\left[\sum_{j=0}^{i-1} \hat{\bar{C}}_{m_j} l_j E_f + (2i-1) r\right] U}{\sum_{j=0}^{n+1} \hat{\bar{C}}_{m_j} l_j E_f + 2nr} \tag{C13}$$

in which the average compliance matrices obtained using the constitutive parameters $\hat{\boldsymbol{\theta}}$ are denoted by $\hat{\bar{C}}_{m_i}$. Equating Eq. C13 to Eq. C11, there is:

$$\bar{C}_{m1} l_1 - 2\bar{C}_{m0} l_0 = \hat{\bar{C}}_{m1} l_1 - 2\hat{\bar{C}}_{m0} l_0 \tag{C14}$$

$$\bar{C}_{m(i+1)} l_{i+1} - \bar{C}_{mi} l_i = \hat{\bar{C}}_{m(i+1)} l_{i+1} - 2\hat{\bar{C}}_{mi} l_i \tag{C15}$$

According to the Cauchy mean value theorem, there exist $\xi_0 \in [\min\{l_0, l_1/2\}, \max\{l_0, l_1/2\}]$, $\xi_1 \in [\min\{l_1/2, l_2/2\}, \max\{l_1/2, l_2/2\}], \ldots \xi_{n-1} \in [\min\{l_{n-1}\ /2, l_n/2\}, \max\{l_{n-1}/2, l_n/2\}]$ which transforms Eq. C14, C15 into:

$$E_m\left(\xi_i; \boldsymbol{\theta}\right) = E_m\left(\xi_i; \hat{\boldsymbol{\theta}}\right) \tag{C16}$$

The identifiability condition is not held if Eq. C16 is satisfied (with $\hat{\boldsymbol{\theta}} \neq \boldsymbol{\theta}$) within the interval of $\xi_0 \in [\min\{l_0, l_1/2\}, \max\{l_0, l_1/2\}]$, $\xi_i \in [\min\{l_i/2, l_{i+1}\ /2\}, \max\{l_i/2, l_{i+1}/2\}], i = 1, 2 \ldots n-1$. If $l_i = l_{i+1}, i = 1, 2 \ldots n-1$, Eq. C16 is unconditionally satisfied, indicating that the identifiability condition is not held for the specimen with uniform resin length (indicated in left figure in Fig. C1b). If $l_i \neq l_{i+1}, i = 1, 2 \ldots n-1$, there exist diverse sizes of resin parts and the satisfaction of Eq. C16 depends on the existence of intersection points between $E_m\left(y; \boldsymbol{\theta}\right)$ and $E_m\left(\xi_i; \hat{\boldsymbol{\theta}}\right)$. Assume that the number of the resin parts with unique lengths within the specimen is q and the maximum number of intersection points between $E_m\left(\xi_i; \boldsymbol{\theta}\right)$ and $E_m\left(\xi_i; \hat{\boldsymbol{\theta}}\right)$ is p. If $p \geq q-1$, Eq. C16 is then satisfied at all the intervals and the identifiability condition is not held (shown in middle figure in Fig. C1b). If $p < q-1$, Eq. C16 cannot be satisfied at some intervals (e.g., $[l_1/2, l_2/2]$ in the right figure of Fig. C1b) and the identifiability condition is satisfied.

References

[1] Abou MY, Jacquemin F, Boyard N, et al (2010) Material characterization and residual stresses simulation during the manufacturing process of epoxy matrix composites. Composites Part A: Applied Science and Manufacturing 41(1):108–115

[2] Aswani A, Shen ZJM, Siddiq A (2018) Inverse optimization with noisy data. Operations Research 66(3):870–892. arXiv:1507.03266

[3] Bogdanor MJ, Oskay C (2017) Prediction of progressive damage and strength of im7/977-3 composites using the eigendeformation-based homogenization approach: Static loading. Journal of Composite Materials 51(10):1455–1472

[4] Bogdanor MJ, Oskay C (2017) Prediction of progressive fatigue damage and failure behavior of IM7/977-3 composites using the reduced-order multiple space-time homogenization approach. Journal of Composite Materials 51(15):2101–2117

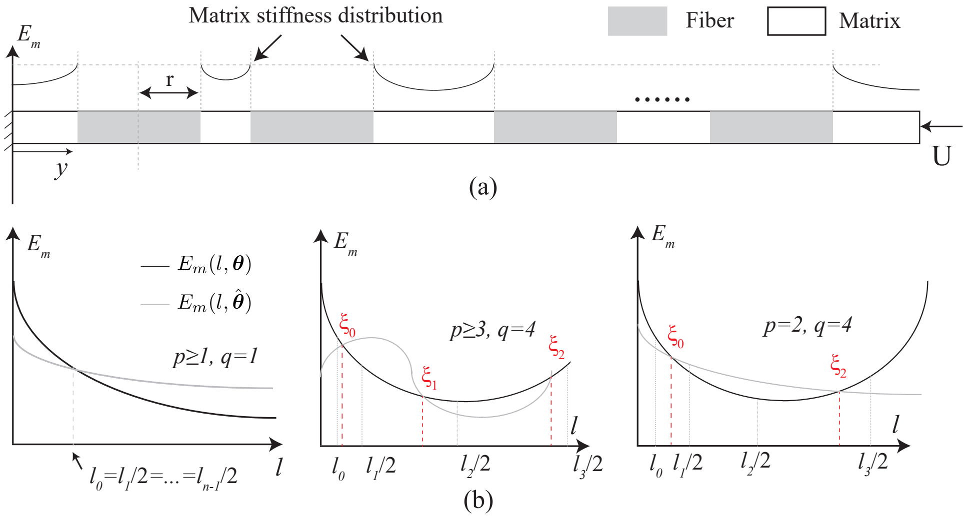

Fig. C1: (a) Schematic illustration of 1D composite specimens. (b) The three cases for the specimen with uniform resin length (left), with diverse resin length and $p \geq q - 1$ (middle), $p < q - 1$ (right). The identifiability condition is not satisfied for the left and middle cases.

[5] Bogdanor MJ, Mahadevan S, Oskay C (2013) Uncertainty quantification in damage modeling of heterogeneous materials. Int J Mult Comp Eng 11:289–307

[6] Bogdanor MJ, Oskay C, Clay SB (2015) Multiscale modeling of failure in composites under model parameter uncertainty. Computational Mechanics 56(3):389–404

[7] Boggs PT, Tolle JW (2000) Sequential quadratic programming for large-scale nonlinear optimization. Journal of Computational and Applied Mathematics 124(1-2):123–137

[8] Boyd S, Boyd SP, Vandenberghe L (2004) Convex Optimization. Cambridge university press

[9] Canal LP, González C, Molina-Aldareguía JM, et al (2012) Application of digital image correlation at the microscale in fiber-reinforced composites. Composites Part A: Applied Science and Manufacturing 43(10):1630–1638

[10] Chevalier J, Camanho PP, Lani F, et al (2019) Multi-scale characterization and modelling of the transverse compression response of unidirectional carbon fiber reinforced epoxy. Composite Structures 209(July 2018):160–176

[11] Creveling PJ, Whitacre WW, Czabaj MW (2019) A fiber-segmentation algorithm for composites imaged using X-ray microtomography: Development and validation. Composites Part A: Applied Science and Manufacturing 126(August):105606

[12] Crouch R, Oskay C, Clay SB (2013) Multiple spatio-temporal scale modeling of composites subjected to cyclic loading. Computational Mechanics 51(1):93–107

[13] Crouch RD, Clay SB, Oskay C (2013) Experimental and computational investigation of progressive damage accumulation in cfrp composites. Composites Part B: Engineering 48:59–67

[14] Czabaj MW, Riccio ML, Whitacre WW (2014) Numerical reconstruction of graphite/epoxy composite microstructure based on sub-micron resolution X-ray computed tomography. Composites Science and Technology 105:174–182

[15] Dhondt G (2021) CalculiX CrunchiX User's Manual version 2.19

[16] Doyley MM (2012) Model-based elastography: a survey of approaches to the inverse elasticity problem. Physics in Medicine & Biology 57(3):R35

[17] D'Mello RJ, Waas AM (2017) Virtual curing of textile polymer matrix composites. Composite Structures 178:455–466

[18] Frankland SJV, Harik VM, Odegard GM, et al (2003) The stress–strain behavior of polymer–nanotube composites from molecular dynamics simulation. Composites Science and Technology 63(11):1655–1661

[19] Gregory JR, Spearing SM (2005) Nanoindentation of neat and in situ polymers in polymer-matrix composites. Composites Science and Technology 65(3-4):595–607

[20] Hardiman M, Vaughan TJ, McCarthy CT (2012) The effect of fibre constraint in the nanoindentation of fibrous composite microstructures: A finite element investigation. Computational Materials Science 64:162–167

[21] Hardiman M, Vaughan TJ, McCarthy CT (2015) Fibrous composite matrix characterisation using nanoindentation: The effect of fibre constraint and the evolution from bulk to in-situ matrix properties. Composites Part A: Applied Science and Manufacturing 68:296–303

[22] Hu Z, Farahikia M, Delfanian F (2015) Fiber bias effect on characterization of carbon fiber-reinforced polymer composites by nanoindentation testing and modeling. Journal of Composite Materials 49(27):3359–3372

[23] Jennrich RI (1969) Asymptotic properties of non-linear least squares estimators. The Annals of Mathematical Statistics 40(2):633–643

[24] Khanna SK, Ranganathan P, Yedla SB, et al (2003) Investigation of nanomechanical properties of the interphase in a glass fiber reinforced polyester composite using nanoindentation. Journal of Engineering Materials and Technology, Transactions of the ASME 125(2):90–96

[25] Kim JK, Sham ML, Wu J (2001) Nanoscale characterisation of interphase in silane treated glass fibre composites. Composites Part A: Applied Science and Manufacturing 32(5):607–618

[26] Kraft D (1988) A software package for sequential quadratic programming. Forschungsbericht- Deutsche Forschungs- und Versuchsanstalt fur Luft- und Raumfahrt

[27] Martí R, Resende MGC, Ribeiro CC (2013) Multi-start methods for combinatorial optimization. European Journal of Operational Research 226(1):1–8

[28] Mehdikhani M, Aravand M, Sabuncuoglu B, et al (2016) Full-field strain measurements at the micro-scale in fiber-reinforced composites using digital image correlation. Composite Structures 140:192–201

[29] Mehdikhani M, Breite C, Swolfs Y, et al (2021) Digital volume correlation for meso/micro in-situ damage analysis in carbon fiber reinforced composites. Composites Science and Technology 213:108944

[30] Michopoulos JG, Hermanson JG, Iliopoulos A, et al (2011) On the constitutive response characterization for composite materials via data-driven design optimization. In: International Design Engineering Technical Conferences and Computers and Information in Engineering Conference, pp 499–511

[31] Oskay C, Fish J (2008) On calibration and validation of eigendeformation-based multiscale models for failure analysis of heterogeneous systems. Computational Mechanics 42(2):181–195

[32] Oskay C, Su Z, Kapusuzoglu B (2020) Discrete eigenseparation-based reduced order homogenization method for failure modeling of composite materials. Computer Methods in Applied Mechanics and Engineering

359:112656

[33] Pecora M, Smerdova O, Gigliotti M (2020) In-situ characterization of the local mechanical behaviour of polymer matrix in 3D carbon fiber composites by cyclic indentation test. Composite Structures 244(March):112268

[34] Rahul RR.and Kitey (2016) Effect of cross-linking on dynamic mechanical and fracture behavior of epoxy variants. Composites Part B: Engineering 85:336–342

[35] Rodríguez M, Molina-Aldareguía JM, González C, et al (2012) Determination of the mechanical properties of amorphous materials through instrumented nanoindentation. Acta Materialia 60(9):3953–3964

[36] Rudin W, et al (1976) Principles of Mathematical Analysis, vol 3. McGraw-Hill New York

[37] Sanei SHR, Barsotti EJ, Leonhardt D, et al (2017) Characterization, synthetic generation, and statistical equivalence of composite microstructures. Journal of composite materials 51(13):1817–1829

[38] Sriramula S, Chryssanthopoulos MK (2009) Quantification of uncertainty modelling in stochastic analysis of frp composites. Composites Part A: Applied Science and Manufacturing 40(11):1673–1684

[39] Strang G, Fix GJ (1973) An Analysis of the Finite Element Method. Englewood Cliffs, N J, Prentice-Hall, Inc, 1973 318 p

[40] Su Z, Oskay C (2021) Mesh size objective fatigue damage propagation in laminated composites using the multiscale discrete damage theory. Computational Mechanics 67(3):969–987

[41] Sun QP, Meng ZX, Zhou GW, et al (2018) Multi-scale computational analysis of unidirectional carbon fiber reinforced polymer composites under various loading conditions. Composite Structures 196(March):30–43

[42] Tabiai I, Texier D, Bocher P, et al (2020) In-situ Full Field Out of Plane Displacement and Strain Measurements at the Micro-Scale in Single Reinforcement Composites under Transverse Load. Experimental Mechanics 60(3):359–377

[43] Tan EPS, Ng SY, Lim CT (2005) Tensile testing of a single ultrafine polymeric fiber. Biomaterials 26(13):1453–1456

[44] Totry E, Molina-Aldareguía JM, González C, et al (2010) Effect of fiber, matrix and interface properties on the in-plane shear deformation of carbon-fiber reinforced composites. Composites Science and Technology 70(6):970–980

[45] Tschopp MA, Wilks GB, Spowart JE (2008) Multi-scale characterization of orthotropic microstructures. Modelling and Simulation in Materials Science and Engineering 16(6):065009

[46] Vaughan TJ, McCarthy CT (2011) A micromechanical study on the effect of intraply properties on transverse shear fracture in fibre reinforced composites. Composites Part A: Applied Science and Manufacturing 42(9):1217–1228

[47] Vigliotti A, Csányi G, Deshpande VS (2018) Bayesian inference of the spatial distributions of material properties. Journal of the Mechanics and Physics of Solids 118:74–97

[48] Virtanen P, Gommers R, Oliphant TE, et al (2020) SciPy 1.0: Fundamental Algorithms for Scientific Computing in Python. Nature Methods 17:261–272

[49] Wang M, Dutta D, Kim K, et al (2015) A computationally efficient approach for inverse material characterization combining gappy pod with direct inversion. Computer Methods in Applied Mechanics and Engineering 286:373–393

[50] Wang YQ, Sutton MA, Bruck HA, et al (2009) Quantitative error assessment in pattern matching: effects of intensity pattern noise, interpolation, strain and image

contrast on motion measurements. Strain 45(2):160–178

[51] Xu J, Wong TC, Simon MA, et al (2022) A clinically applicable strategy to estimate the in vivo distribution of mechanical material properties of the right ventricular wall. International Journal for Numerical Methods in Biomedical Engineering 38(2):e3548

[52] Yang C, Feng H, Xu Z, et al (2018) The spatial correlation problem of noise in imaging deblurring and its solution. Journal of Visual Communication and Image Representation 56:167–176

[53] Zhandarov S, Mäder E (2005) Characterization of fiber/matrix interface strength: applicability of different tests, approaches and parameters. Composites Science and Technology 65(1):149–160